

Comparing Lensing and Stellar Orbital Models of a Nearby Massive Strong-Lens Galaxy

Adriano Poci^{1*}, Russell J. Smith¹

¹*Centre for Extragalactic Astronomy, University of Durham, Stockton Road, Durham DH1 3LE, United Kingdom*

Accepted XXX. Received YYY; in original form ZZZ

ABSTRACT

Exploiting the relative proximity of the nearby strong-lens galaxy SNL-1, we present a critical comparison of the mass estimates derived from independent modelling techniques. We fit triaxial orbit-superposition dynamical models to spatially-resolved stellar kinematics, and compare to the constraints derived from lens modelling of high-resolution photometry. From the dynamical model, we measure the total (dynamical) mass enclosed within a projected aperture of radius the Einstein radius to be $\log_{10}(M_{\text{Ein.}}/M_{\odot}) = 11.00 \pm 0.02$, which agrees with previous measurements from lens modelling to within 5%. We then explore the intrinsic (de-projected) properties of the best-fitting dynamical model. We find that SNL-1 has approximately-constant, intermediate triaxiality at all radii. It is oblate-like in the inner regions (around the Einstein radius) and tends towards spherical at larger radii. The stellar velocity ellipsoid gradually transforms from isotropic in the very central regions to radially-biased in the outskirts. We find that SNL-1 is dynamically consistent with the broader galaxy population, as measured by the relative fraction of orbit ‘temperatures’ compared to the CALIFA survey. On the mass–size plane, SNL-1 occupies the most-compact edge given its mass, compared to both the MaNGA and SAMI surveys. Finally, we explore how the observed lensing configuration is affected by the orientation of the lens galaxy. We discuss the implications of such detailed models on future combined lensing and dynamical analyses.

Key words: galaxies: elliptical and lenticular, cD – galaxies: structure – galaxies: kinematics and dynamics – galaxies: stellar content

1 INTRODUCTION

The mass of a galaxy is one of the most critical properties controlling its evolution over cosmic time. This is evidenced by the plethora of observed correlations of other galactic properties with mass (e.g. Gallazzi et al. 2005; Cortese et al. 2014; Barone et al. 2021; Tian et al. 2021). Measuring the mass, however, is notoriously difficult for a number of reasons. Transforming the observed luminosity of a galaxy into a baryonic mass is prone to systematic uncertainties relating to distances, the underlying stellar populations, and complications such as dust. Moreover, a significant portion of a galaxy’s mass, the dark matter (DM), is completely invisible and therefore must be inferred from its effect on luminous matter.

Direct probes of the gravitational potential can circumvent many of these issues, and can constrain the total (gravitational) mass, irrespective of the specific combination of baryonic and dark matter. To this end, gravitational lensing

offers a relatively assumption-independent avenue for constraining the total enclosed mass within the characteristic Einstein radius $\theta_{\text{Ein.}}$ (e.g. Chae 2003; Treu 2010). Moreover, in general, the confidence with which a lensing model can be constrained is dependent on the geometry and multiplicity of the images produced (e.g. Shu et al. 2015; Smith et al. 2018). Finally, the main degeneracy in lensing models — in particular those with only two lensed images and/or little spatial structure in the images — is between the mass which is responsible for the lensing, and contributions from external effects (e.g. the degeneracy between mass and shear). However with high-quality data, this degeneracy can in principle be overcome by using the flux information in the pixels of the source images, rather than just their positions around the lens (Collier et al. 2018). Unfortunately lensing analyses are naturally limited to the small samples of galaxies which are acting as strong lenses to background sources (e.g. Bolton et al. 2006), and so mass census of the galaxy population using this technique is similarly limited.

Kinematics of the baryonic components can also provide robust estimates of the total enclosed mass of galaxies,

*E-mail: adriano.poci@durham.ac.uk

since they directly trace the total gravitational potential (irrespective of the specific combination of baryons and DM). However, measuring kinematics requires spectroscopy with relatively high signal-to-noise (S/N), which is considerably more expensive than photometry, especially at the redshift of typical strong-lens systems. This requirement tightens with increasing generality of the dynamical model employed.

Comparing the measurements of the projected enclosed mass for the same galaxy provides a critical test of these two techniques, and consequently whether previous works using either technique are directly comparable. Dynamical models have in fact been applied to a sample of lensed galaxies, finding that models with DM better match the lensing analyses compared to mass-follows-light models (Thomas et al. 2011). Using the lens sample from the Sloan Lens ACS Survey (SLACS; Bolton et al. 2006), two-integral dynamical models were explored using spatially-resolved stellar kinematics (Czoske et al. 2008; Barnabè et al. 2009, 2011). However, given the relatively large distances to the majority of strong lens galaxies (for instance, SLACS sample is at $0.08 < z < 0.35$, with the most massive around $z \sim 0.25$), the available data make detailed dynamical modelling challenging. These analyses (e.g. Treu & Koopmans 2004; Koopmans et al. 2009; Auger et al. 2010; Thomas et al. 2011) more often rely on mass estimators which require only a central velocity dispersion (such as in Cappellari et al. 2006; Wolf et al. 2010; Campbell et al. 2017, and their respective assumptions). The sample of lenses collected as part of the SINFONI Nearby Elliptical Lens Locator Survey (SNELLS; Smith et al. 2015) is unique for the relatively small distances to the lens galaxies. Newman et al. (2017) have exploited their proximity to derive combined constraints from stellar-population and lensing analyses for a subset of the SNELLS galaxies in order to measure potential variations of the stellar Initial Mass Function (IMF).

In this work, we also take advantage of the distances of the SNELLS galaxies to conduct a detailed dynamical analysis and comparison to constraints from lens modelling for SNL-1 (ESO286-G022). We compute triaxial three-integral orbit-based dynamical models of SNL-1 using the measured spatially-resolved kinematic moments which do not require specific assumptions regarding the mass distribution or orbital anisotropy. For consistency with the lens modelling of Collier et al. (2018) — to which we directly compare the dynamical modelling results — we assume the cosmology of the *Wilkinson Microwave Anisotropy Probe* (WMAP) 7-year experiment (Komatsu et al. 2011). Physical properties of SNL-1 are summarised in Table 1.

2 DATA & TARGET

The dynamical model used in this work (Section 3) requires high-quality photometry and spectroscopy in order to be robustly constrained. We utilise Hubble Space Telescope (*HST*) Advanced Camera for Surveys (ACS) photometry in order to derive a model for the projected surface brightness of SNL-1, which is used as the tracer distribution for the dynamical model. Very Large Telescope (VLT) Multi-Unit Spectroscopic Explorer (MUSE) integral-field unit (IFU) spectroscopy is used to measure the stellar kinematics and star-formation history. The stellar kinematics will constrain

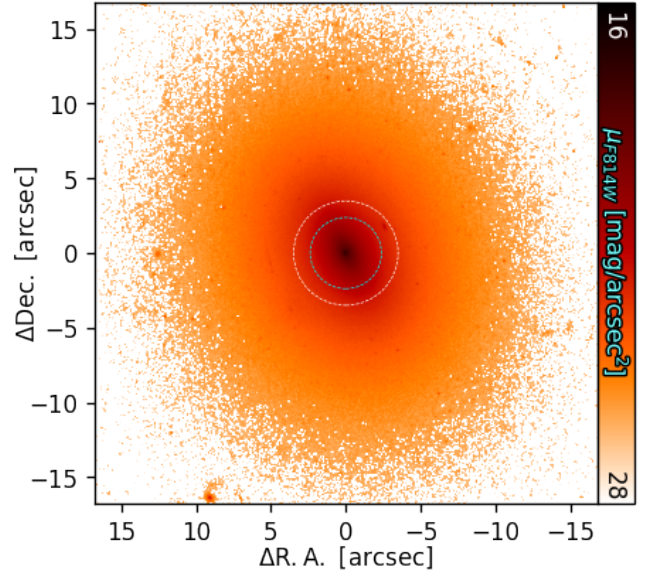


Figure 1. $F814W$ image of SNL-1. Circular apertures with radii R_e and θ_{Ein} are shown in white and cyan, respectively.

the dynamical model directly, while the stellar populations will be used to derive a stellar mass model from the surface brightness.

2.1 Photometry

Collier et al. (2018) presented observations of SNL-1 in the $F336W$ and $F814W$ bands of *HST*/ACS. From these data, we utilised the $F814W$ band with an exposure time of 1050 s, as it is deeper than the $F336W$ and consistent with the wavelength range of the spectroscopy. The $F814W$ image is shown in Fig. 1. We also have r -band data from FORS2 which we utilise for auxiliary investigations below. However, given the lower spatial resolution and non-uniform sky background of this data, we opt for the *HST* $F814W$ for the main modelling of this work.

2.2 Spectroscopy

The spectroscopy of SNL-1 was obtained using MUSE in the wide-field mode (WFM) configuration without adaptive optics, with program ID 0100.B-0769(A). These data have an exposure time of 1180 s. They were reduced via the standard ESO MUSE pipeline. At the derived distance to SNL-1, the 0.2 arcsec/pixel resolution of these data translate into a physical spatial resolution of 124 pc, but with an estimated point-spread function (PSF) of $\sim 1''$ (~ 621 pc) full-width half-maximum.

The MUSE data-cube was spatially binned to a target signal-to-noise $S/N = 50$ using a Python implementation¹ of the Voronoi binning algorithm (Cappellari & Copin 2003). This S/N was chosen as a compromise between being able to robustly extract higher-order information from the spectral fits, and maintaining sufficient spatial sampling across the FOV in order to preserve the kinematic structures. For

¹ Available at <https://pypi.org/project/vorbin/>

Redshift	z	0.0312	Smith et al. (2015)
Einstein radius	$\theta_{\text{Ein.}}$	2.38'' 1.48 kpc	Smith et al. (2015)
Total mass	$\log_{10}(M/M_{\odot})$	10.98	Collier et al. (2018)
Distance	D	132 Mpc 128 Mpc	co-moving angular diameter
Effective radius	R_e^{F814W}	3.49'' 2.15 kpc	—

Table 1. Physical properties of SNL-1 from the literature and this work.

all data products, we consider the rest-frame spectral range $\lambda \in [4700, 6700]$ Å, as red-ward of 6700 Å, the data are more noisy and contain sky emission lines. The binned data extend out to $r_{\text{max}} = 9.67''$ (6.01 kpc) or $\sim 2.7 R_e$. To measure the stellar population properties, the binned spectra were fit using the E-MILES⁴ single stellar population (SSP) templates (Vazdekis et al. 2016) within PPXF² (Cappellari 2008, 2017). Specifically, we used the models computed using the ‘BaSTI’ isochrones (Pietrinferni et al. 2004), with ‘base’ (Solar neighbourhood) elemental abundances, and a fixed ‘revised’ Kroupa (2001) IMF over the safe ranges of age (t) and total metallicity ($[Z/H]$)³. We included a multiplicative polynomial of order 12 to account for any mismatch between the absolute flux calibrations of the data and models, and any residual stellar continuum not accounted for by the models. A linear regularisation term ($\Delta = 10$) was also included, which favours a smooth SSP weight distribution in the underlying $t - [Z/H]$ space given otherwise degenerate solutions.

We used the resulting distribution of age and metallicity in each spatial bin to compute the $F814W$ -band stellar mass-to-light ratio (M_*/L_{F814W}). For the stellar mass, the E-MILES predictions including the mass in stars and stellar remnants was used. To compute the luminosity, we used the SSP model spectra directly. First, we took each SSP template which was assigned non-zero weight in the fit, and computed the absolute magnitude by applying the $F814W$ filter response curve redshifted to the distance of SNL-1. We then took the standard Solar spectrum of Colina et al. (1996) from the *HST* CALSPEC database (Bohlin et al. 2014, 2020) and computed its magnitude in the same way. In this way, we computed the total luminosity by weighting the individual SSP luminosities according to the weights of the spectral fit. The 2D map of M_*/L_{F814W} is shown in the inset of Fig. 2.

Measurements of the stellar kinematics were also made from the same data, in this instance fitting the spectra again in PPXF using the MILES⁴ empirical stellar library (Sánchez-Blázquez et al. 2006; Falcón-Barroso et al. 2011). We employ stellar spectra for this fit because they have higher intrinsic resolution compared to the SSP models, which improves the fit to complex absorption-line shapes. In this instance, an additive polynomial of order 12 was included to ensure that the shapes of the absorption features are accurately reproduced, and no regularisation of the weights is imposed. In order to robustly constrain the dynamical model (Section 3), we measured the first four

Gauss-Hermite moments of the line-of-sight velocity distribution (LOSVD), shown in the top row of Fig. 3.

During the fit to every spectrum, bad spectral pixels were iteratively clipped. This efficiently masks emission (which is not accounted for in the fitting), any sky lines, and other spurious artefacts in the spectrum. This scheme would also account for any emission from the source galaxy, as well as template mismatch during the fitting. Since the lensed images are undetected in continuum, no spatial masking is required.

3 DYNAMICAL MODEL

In this work we aim to construct an accurate dynamical model in order to derive constraints which are in line with those produced from the lensing analysis. Since the latter is subject to few assumptions, we also wish to minimise those imposed on the dynamical model. We therefore apply a highly-general orbit-superposition technique built on the original premise of Schwarzschild (1979). We utilise the triaxial three-integral implementation described in van den Bosch et al. (2008); van de Ven et al. (2008); Zhu et al. (2018a), and validated on mock data in Jin et al. (2019). This technique allows for freedom in the shape of the velocity ellipsoid and intrinsic mass distribution. Confronting this method with the result from lensing provides a critical test of the ingredients that are required to fit the observational data. We first briefly describe those ingredients here.

3.1 Projected Mass Model

Dynamical models require a description of the mass distribution in order to compute kinematic predictions, but this is not a direct observable. In practise, the mass distribution is derived from some projected constraints, then deprojected into an intrinsic distribution via specific assumptions about the shape of the galaxy. In this work, we computed a model of the projected surface brightness by fitting a multi-Gaussian Expansion (MGE; Monnet et al. 1992; Emsellem et al. 1994) to the $F814W$ photometry using a Python implementation⁵ (Cappellari 2002). To convert this fit into physical units we took into account the surface-brightness dimming due to redshift, Galactic extinction according to Schlafly & Finkbeiner (2011), as well as a K-correction in the redshifted $F814W$ band. This model describes the projected distribution of the visible tracer of the underlying

² Available at <https://pypi.org/project/ppxf/>

³ as defined at <http://research.iac.es/proyecto/miles/pages/ssp-models/safe-ranges.php>

⁴ Available at <http://research.iac.es/proyecto/miles/>

⁵ Available at <https://pypi.org/project/mgefit/>

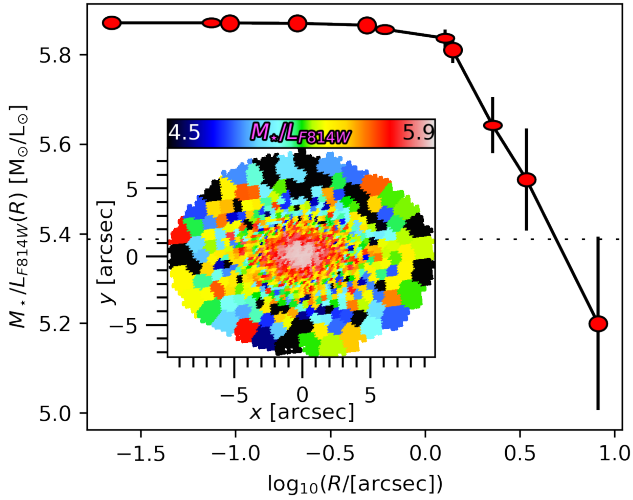


Figure 2. *Main:* Azimuthally-sampled radial profile of the measured M_*/L_{F814W} from the full spectral fitting in Section 2.2. The measurements are sampled in a thin annulus around the location (σ) of every Gaussian of MGE_μ (see text). The data points depict the shape of the annulus taken for each Gaussian component, governed by its axis ratio. The vertical ‘error bars’ illustrate the range of M_*/L within each annulus. The black dashed line shows the average value of M_*/L_{F814W} over the individual Voronoi bins. *Inset:* The spatially-resolved map of M_*/L_{F814W} .

gravitational potential. Since it describes the surface brightness, we refer to it is MGE_μ .

We still require, however, a description of the mass. To this end, we utilise the spectroscopic M_*/L_{F814W} in order to convert the stellar luminosity into mass. This is achieved following the approach of Poci et al. (2017), which we outline here (with similar approaches from Li et al. 2017; Mitzkus et al. 2017; Yang et al. 2020). Since MGE_μ is constructed from the co-addition of overlapping 2D Gaussians of different projected shapes, widths, and intensities, we derived the corresponding M_*/L for each Gaussian individually. For each Gaussian, we took a thin projected annulus centred at its ‘width’ (radial extent) and with the same axis ratio, and calculated the mean M_*/L from the pPXF stellar-population fit within that annulus. The mean value is then the factor which converts the luminosity of that Gaussian into mass. The final set of scaled Gaussians represents a projected mass model, which we denote MGE_Σ . In this implementation, the tailored azimuthal sampling naturally accounts for the interplay between the individual Gaussians and the changing shape of the light distribution with radius. This allows the dynamical model to account for the spatial variations of M_*/L driven by age and metallicity variations, notwithstanding the evidence for internal IMF variations in massive ETGs similar to SNL-1 (e.g. van Dokkum et al. 2017; Vaughan et al. 2018; La Barbera et al. 2019). Given the spheroidal geometry of SNL-1, we expect radial profiles to capture these variations. The 2D map and resulting radial profile of the measured M_*/L_{F814W} are shown in Fig. 2, and both MGE_μ and MGE_Σ are tabulated in appendix A. With respect to the spatially-averaged value denoted in Fig. 2, it can be seen that explicitly including the radial profile in our mass model accounts for the $\sim \pm 10\%$ variations of M_*/L_{F814W} caused by age and metallicity gradients.

3.2 Intrinsic Parameter Space Exploration

The goal of the dynamical model is to find the best set of intrinsic (de-projected) properties which reproduce both the projected mass distribution and the observed (projected) stellar kinematics. The specific implementation of the Schwarzschild method used here describes the intrinsic mass distribution with seven parameters:

- a parametrisation of the intrinsic shape of the stellar component with three axis ratios $q = C/A$, $p = B/A$, and $u = A'/A$, where A , B , and C are the intrinsic major, intermediate, and minor axes, respectively, and A' is the projected major axis
- the mass of the central SMBH, M_\bullet . This is implemented as a ‘dark’ mass following a Plummer density profile (Dejonghe 1987)
- two parameters describing the DM halo, assumed to be a spherical Navarro-Frenk-White (NFW) model (Navarro et al. 1996). These are the concentration C_{DM} and dark mass fraction at r_{200} , f_{DM}
- a global dynamical mass-to-light ratio. We denote this quantity Υ to distinguish from the spectroscopic M_*/L . Υ deepens or flattens the global gravitational potential, resulting in larger or smaller velocities, respectively, as needed to fit the kinematics. It can account for systematic effects caused by the absolute calibration of the SSP models, the particular choice of IMF, and/or the assumption of a spherical NFW DM halo.

For a single set of the above parameters, a large library of representative orbits are numerically integrated within the corresponding gravitational potential. The orbits conserve three integrals of motions: E , I_2 , and I_3 . Our models sample these integrals in 25 logarithmic steps for E , 18 linear steps for I_2 , and 10 linear steps for I_3 . To avoid discreteness (aliasing) in the models, each (E, I_2, I_3) location was ‘dithered’ (as in Cappellari et al. 2006) by a factor of 5. This creates a cloud of orbits with adjacent initial conditions for every integration, alleviating any possible discreteness in the model observables without having to integrate five times as many orbits.

The complete orbit library was fit to the measured kinematics via a Non-Negative Least-Squares (NNLS; Lawson & Hanson 1995) algorithm. As a boundary constraint, the orbits are also required to reproduce the projected luminosity (MGE_μ). During this fit, a linear regularisation is imposed – analogous to that used for spectral fitting – in this case favouring smooth distributions in the orbital phase-space (E, I_2, I_3) . The result of the NNLS fit is a set of (luminosity) weights for all of the integrated orbits, whose weighted combination reproduces all of the kinematic observables.

It is then necessary to explore many possible sets of parameters – different intrinsic gravitational potentials – at each stage finding the best subset of orbits via NNLS. Each model consists of 6 gravitational parameters: M_\bullet , q , p , u , C_{DM} , and f_{DM} , where each set is evaluated in NNLS over a range of Υ (since changing Υ does not require re-integration of the orbits). We note here, however, that using the measured velocity dispersion within the effective radius, σ_e , and the $M_\bullet - \sigma_e$ relation of Kormendy & Ho (2013), we estimate the radius of the sphere-of-influence for the given M_\bullet to be $r = 0.12''$ – well below the MUSE PSF. Therefore,

Parameter	Description	Best	1σ
$\log_{10}(M_{\bullet}/M_{\odot})$	Black-Hole Mass	9.36	1.089
q	Intrinsic Shape	0.4949	0.0090
p	Intrinsic Shape	0.8390	0.0281
u	Intrinsic Shape	0.9910	0.0026
θ'	Viewing Angle	88.05°	
ϕ'	Viewing Angle	75.76°	
ψ'	Viewing Angle	75.76°	
C_{DM}	DM Concentration	21.00	2.67
$\log_{10}[f_{\text{DM}}(r_{200})]$	DM Fraction at r_{200}	2.00	0.094
$\Upsilon[M_{\odot}/L_{\odot}]$	Global M/L	0.66	0.042

Table 2. Free parameters of the Schwarzschild model, their best-fitting values, and the associated uncertainties which are derived as per appendix B. Note that θ' , ϕ' , ψ' are derived from the best-fitting q , p , u .

while we leave M_{\bullet} as a free parameter for completeness, we expect the constraints on it to be weak given our current data. The exploration of the parameter space is described in appendix B. Overall, 7233 unique models were evaluated, and the best fit is shown in Fig. 3.

4 RESULTS

The parameters of the best-fitting Schwarzschild model are given in Table 2. The Schwarzschild model provides a plethora of intrinsic properties, including the 3D shapes of the mass distribution (defined by the parameters in Table 2) and velocity ellipsoid (defined by the specific orbit superposition). One of the important quantities for the test sought here is the projected mass enclosed within a circular aperture of radius $\theta_{\text{Ein.}}$. We compute this in the following way. Each spatial aperture of the kinematic data has an associated luminosity weighting, which is the summation over the weights of all orbits which cross that aperture. We converted the luminosity weights into total mass weights by adding an MGE parametrisation of the best-fitting NFW halo to MGE_{Σ} , then dividing by MGE_{μ} . This scale factor was evaluated at every aperture so that we could compute the fractional dynamical mass from the model. The projected fractional mass weight within $\theta_{\text{Ein.}}$, $f_{\text{Ein.}}$, was then computed by simply summing all apertures with circular (projected) radius $r \leq \theta_{\text{Ein.}}$. Then the enclosed dynamical mass was computed by combining and integrating the enclosed mass profiles of the stars, DM, and SMBH. We integrated these profiles up to the maximum radial extent of the kinematic data, r_{max} , producing an enclosed dynamical mass within the FOV, M_{FOV} . Finally, the projected dynamical mass within $\theta_{\text{Ein.}}$ is given straight-forwardly as $M_{\text{Ein.}} = f_{\text{Ein.}}M_{\text{FOV}}$. The intrinsic enclosed mass profiles, along with the projected measurements from both the dynamical and lensing models, are presented in Fig. 4.

From the inset of Fig. 4, it is clear that the measurements of the projected Einstein mass from the lensing and dynamical models are in excellent agreement with one another, with $(9.49 \pm 0.15) \times 10^{10} M_{\odot}$ and $(9.89 \pm 0.47) \times 10^{10} M_{\odot}$, respectively. The uncertainty on the result from the dynamical model is computed by repeating the measurement for every model evaluation within 1σ of the best-fit solution, and finding the variance. While the dynamical mass is expected to be a robust quantity, this outcome is still

reassuring in light of the generality and complexity of the Schwarzschild model, and given that the lensing and dynamical masses were completely independent of one another. By establishing that the Schwarzschild model is accurately anchored to the lensing result at $\theta_{\text{Ein.}}$, we can then confidently explore the other properties and spatial regions of the model in more detail. The intrinsic enclosed mass profiles shown in Fig. 4 illustrate that SNL-1 is completely baryon-dominated within $\theta_{\text{Ein.}}$. Enclosed within r_{max} , we measure a total stellar mass of $\log_{10}(M_{\star}/M_{\odot}) = 11.23$, and a dynamical mass of $\log_{10}(M_{\text{dyn.}}/M_{\odot}) = 11.41$. Enclosed within R_e , we measure $\log_{10}(M_{\star}/M_{\odot}) = 11.01$ and $\log_{10}(M_{\text{dyn.}}/M_{\odot}) = 11.07$, implying a DM fraction $f_{\text{DM}}(r \leq R_e) = 10.67\%$. It is clear that SNL-1 is baryon-dominated within the spectroscopic FOV.

The intrinsic shape of SNL-1 is explored in Fig. 5 as a function of radius. This figure shows the radial dependence of the correlation between p^2 and q^2 . In this way, the gradient of the curve is also approximately related to the triaxiality parameter (Franx et al. 1991), $T \equiv (1 - p^2)/(1 - q^2)$. Strictly, our model of SNL-1 is triaxial at all radii. However $p = B/A \gtrsim 0.9$ for all radii implying only minor triaxiality. Jin et al. (2020) quantitatively categorises galaxies as oblate-triaxial, triaxial, and prolate-triaxial for $T < 0.3$, $0.3 < T < 0.7$ and $0.7 < T$, respectively. The mean triaxiality within the FOV for our model of SNL-1 is $\langle T \rangle = 0.39$, implying that it is oblate-triaxial. Interestingly, q is smallest around $\theta_{\text{Ein.}}$. This also happens to be the region in which the stellar rotation is high, and regularly-rotating galaxies are expected to be oblate (Weijmans et al. 2014), so the value of q is perhaps unsurprising. The outskirts become more spheroidal, coincident with where the rotation diminishes. This could be the result of isotropic minor accretion. Galaxies as massive as SNL-1 are expected to have accreted a large portion of their present-day mass (Oser et al. 2010; Khochfar et al. 2011; Lackner et al. 2012; Rodriguez-Gomez et al. 2016), which would preferentially settle in the outskirts (Karademir et al. 2019) and explain both the intrinsic shape and lack of rotation.

Of further interest is the shape of the intrinsic stellar velocity ellipsoid (SVE). This is particularly important because some dynamical mass estimators — which may also be used in joint lensing analyses — are valid only under the assumption of orbital isotropy. Orbital anisotropy has, however, been indirectly investigated in some lensing studies (e.g. Koopmans et al. 2009). To test this assumption, we investigate the radial variations of anisotropy, for each pair of axes of a cylindrically-aligned SVE. We explore the classic anisotropy parameter (Binney & Tremaine 1987)

$$\beta_{ij} = 1 - \frac{\sigma_i}{\sigma_j} \quad (1)$$

for every $(i, j) \in [R, \phi, z]$. These results are shown in Fig. 6. Within $\theta_{\text{Ein.}}$, SNL-1 may be considered approximately isotropic; $\sigma_R \approx \sigma_{\phi} \approx \sigma_z$ for $r < \theta_{\text{Ein.}}$. At larger radii, SNL-1 becomes increasingly radially biased with increasing radius; $\sigma_z \approx \sigma_{\phi} < \sigma_R$ for $r > \theta_{\text{Ein.}}$. Such anisotropy provides additional evidence of a rich accretion history over which many systems contributed to the build-up of the outer spheroid (e.g. Naab et al. 2006), as has also been found in the Milky-Way (e.g. Helmi et al. 2018). It also indicates that within $\theta_{\text{Ein.}}$, the assumption of orbital isotropy — at least for SNL-1 — would be reasonable.

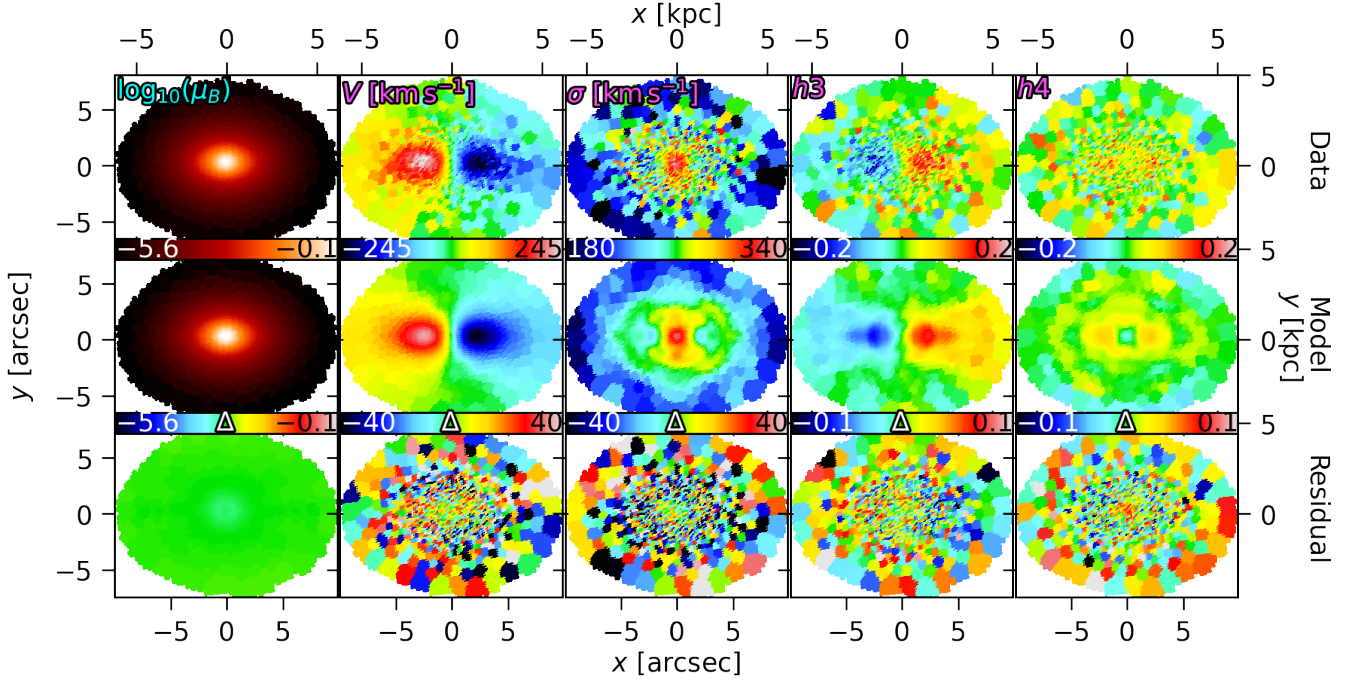


Figure 3. Schwarzschild model fit to the measured kinematics of SNL-1. Data are shown in the top row and the model in the middle row. The residuals ($\Delta = \text{data} - \text{model}$) are shown in the bottom row, with their corresponding colour bars. From left to right, the columns contain the projected surface brightness, mean velocity, velocity dispersion, $h3$, and $h4$.

5 DISCUSSION

The dynamical model has afforded us a detailed look at the resolved internal kinematic properties of SNL-1. We see that the central regions exhibit high rotation, an oblate mass distribution, and approximately-isotropic orbits. The outskirts exhibit little-to-no rotation, a spheroidal mass distribution, and are accompanied by an increase in radially-biased orbits. Intermediate triaxiality persists throughout the galaxy.

5.1 SNL-1 in Context

Apart from being a strong lens, SNL-1 exists within the population of massive elliptical galaxies. It is, however, highly compact for its mass (Campbell et al. 2014; Smith et al. 2015; Spiniello et al. 2015), and therefore may not be representative of the ETG population as a whole. We thus seek to compare it to similar galaxies in order to discern any differences between them. Exploiting the generality of the Schwarzschild model, we can make this comparison for a number of key intrinsic properties.

In Fig. 7, the orbital circularity distribution is shown. The orbital circularity λ_z is a measure of the intrinsic angular momentum around the short axis of the mass distribution (Zhu et al. 2018a). It is normalised by the angular momentum of a circular orbit with equivalent energy, such that $\lambda_z \in [-1, 1]$, representing counter- and co-rotating circular orbits, respectively. Box and/or radial orbits will exhibit $\lambda_z \sim 0$. Fig. 7 shows that SNL-1 is composed of dynamically-hot and -warm orbits with $\lambda_z \lesssim 0.7$. We use this distribution to compare to the analysis conducted on the representative sample of nearby galaxies from the CALIFA survey (Sánchez et al. 2012), which contains a small num-

ber of galaxies of similar mass to SNL-1. Zhu et al. (2018b) applied triaxial Schwarzschild models to that sample and analysed the distribution of orbits as a function of stellar mass by dividing the circularity into broad bins of ‘cold’ ($\lambda_z \geq 0.8$), ‘warm’ ($0.25 < \lambda_z < 0.8$), ‘hot’ ($|\lambda_z| \leq 0.25$), and counter-rotating ($\lambda_z < -0.25$) orbits. They specifically considered the fractions of each orbit type within R_e . Applying these same criteria, we compare orbits fractions to the CALIFA galaxy sample in Fig. 8. The model of SNL-1 reveals cold, warm, hot, and counter-rotating fractions within R_e of 0.07, 0.47, 0.39, and 0.07, respectively. SNL-1 is consistent with the $\log_{10}(M_*/M_\odot) \sim 11$ population of galaxies from CALIFA, in terms of the orbit distributions. Given its mass, SNL-1 is expected to be supported predominantly by random motions (for instance, see Cappellari et al. 2013a), and we see this borne out of our model as a significant fraction of hot orbits at all radii. Simultaneously, SNL-1 exhibits relatively high peak rotation velocity. It can be seen from Fig. 7 that this rotation is produced predominantly by the cloud of dynamically-warm orbits extending from the centre to $\sim 2\text{kpc}$ (since there is negligible contributions from cold orbits), thereby explaining the relatively high warm-orbit fraction within R_e . These orbits would constitute a ‘thick-disk’-like component, embedded in the otherwise spheroidal galaxy.

In contrast to its rather typical dynamical properties, SNL-1 appears to be somewhat unusual structurally, being highly compact for its mass. We therefore investigate its position on the mass–size plane, an empirical correlation believed to capture the various evolutionary stages of a population of galaxies (e.g. Newton et al. 2011; Cappellari et al. 2013a; Cappellari 2013; Scott et al. 2017; Krajnović et al. 2018; Li et al. 2018). In Fig. 9, we place SNL-1 on

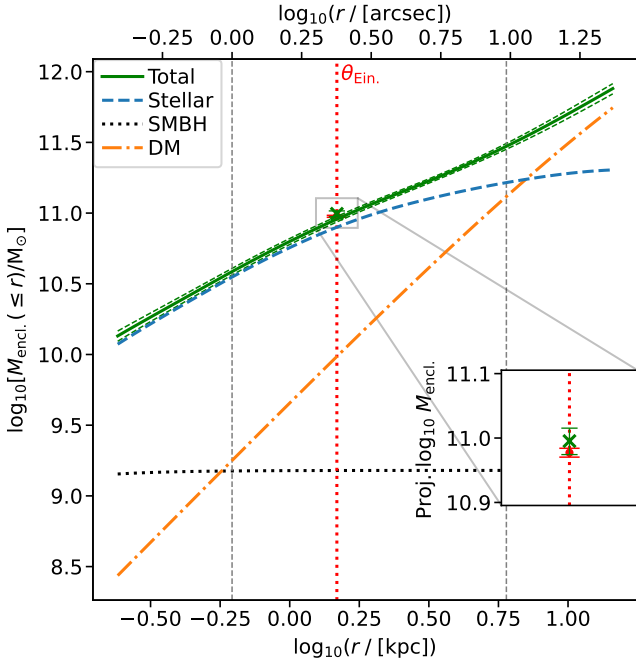


Figure 4. Enclosed mass of SNL-1. Intrinsic de-projected profiles of the enclosed stellar and dark mass are shown in dashed blue and dot-dashed orange, respectively. The total enclosed mass is shown as the green solid line [given by $M_*(r) + M_{DM}(r) + M_\bullet(r)$, although the SMBH is a point source over the radial range considered]. The black-hole mass is shown in dotted grey for reference. The green cross and the red errorbar illustrate the projected constraints from the dynamical and lensing models, respectively. The PSF and largest radial extent of the MUSE data are demarcated by the inner and outer vertical dashed lines, respectively. $\theta_{\text{Ein.}}$ is shown as the red dotted line. For the dynamical model, the errorbar on the cross and the dashed green lines illustrate the spread of all models within 1σ of the best-fitting solution. *Inset:* Zoom-in of the measurements of the projected Einstein mass from the lensing and dynamical models.

both the dynamical-mass-size plane measured in Li et al. (2018) using the MaNGA survey (Bundy et al. 2015), and the stellar-mass-size plane using DR3 (Croom et al. 2021) of the SAMI survey (Croom et al. 2012), comparing also to a sample of ‘relic’ galaxies from the INSPIRE survey (Spiniello et al. 2021). SNL-1 occupies the boundary at the compact, high-mass edge of the ‘normal’ galaxy populations. It resides in the “zone of exclusion”, which was derived dynamically for the ATLAS^{3D} sample of galaxies in the Virgo cluster (Cappellari 2013, but proposed originally by Bender et al. 1992; Burstein et al. 1997). This may be the result of the fact that more compact galaxies are preferentially easier to detect as being strong lenses, as already hinted to in the results of Newton et al. (2011). Moreover, SNL-1 appears to bridge the gap between the relic and non-relic populations, the former being defined specifically by their compactness. This further reinforces the atypical compactness of SNL-1 with respect to the broader galaxy population.

Overall this section has shown that SNL-1 is dynamically typical but structurally atypical compared to galaxies of similar mass. Of particular interest for lensing models which utilise the central velocity dispersions as dynamical tracers, at its Einstein radius SNL-1 exhibits the greatest

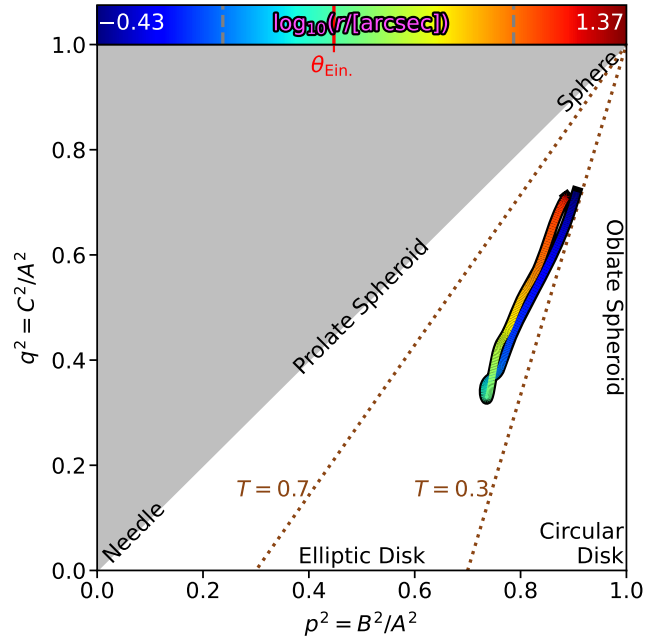


Figure 5. Correlations of the axis ratios of the intrinsic stellar mass distribution. The curve is coloured by radius. The PSF and largest radial extent of the MUSE data are demarcated on the colour bar by the dashed grey lines. $\theta_{\text{Ein.}}$ is also marked on the colour bar. The dotted brown lines illustrate the boundaries between the classes of triaxiality in Jin et al. (2020). The various shape labels are borrowed from de Zeeuw & Schwarzschild (1989). The radial profile illustrates that SNL-1 tends towards a spherical mass distribution at both small and large radii, but exhibits the strongest departure at $\theta_{\text{Ein.}}$. Mild, approximately-constant triaxiality is present throughout the galaxy.

departure from a spherical mass distribution, but no significant departure from orbital isotropy. These results suggest that orientation/configuration biases are likely already manifest in existing lensing samples, while our methodology — specifically the sophisticated orbit-based dynamical models — provides a way to quantify and account for such biases in future samples. In this case, the properties derived from lensing analyses, even if large samples are collected, may not be representative of the broader galaxy population.

5.2 Dynamical Analyses of Lensing Systems

The lensing selection function is of considerable importance, and depends on the projected mass of the lens along the LOS (for which the stellar velocity dispersion is a common proxy; Treu et al. 2010). However, there are other physical properties of the lensing galaxies which would be especially conducive to producing detectable strong-lens signals. For instance, Schaller et al. (2015) studied a sample of galaxy clusters in cosmological hydrodynamical simulations and find that, of their 6 clusters, 4 brightest cluster galaxies are prolate, and 2 are oblate. They argue that if such galaxies were intrinsically prolate, but were selected for observation in such a way which favours end-on orientations, then the measured central velocity dispersion would be biased to higher values compared to a sample with a uniform distribution of orientations. A similar argument could ap-

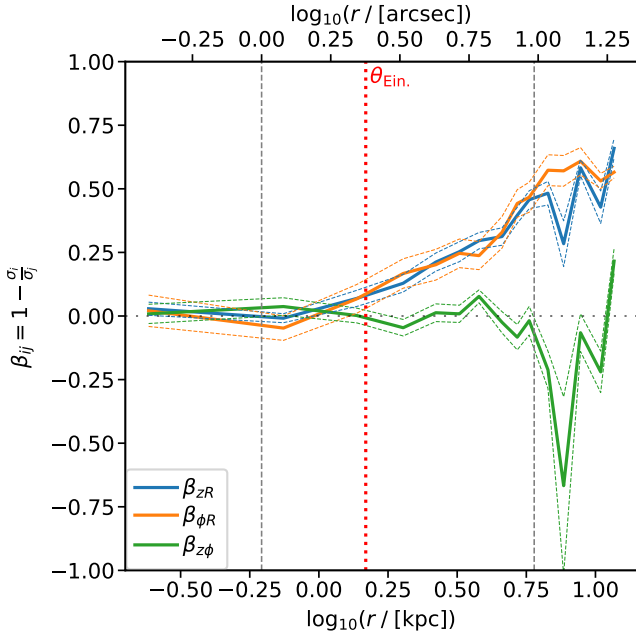


Figure 6. Radial profiles of the intrinsic axes of the stellar velocity ellipsoid. The β_{ij} quantities are defined in Eq. (1). The PSF and largest radial extent of the MUSE data are demarcated by the inner and outer vertical dashed lines, respectively. θ_{Ein} is shown as the red dotted line. The coloured dashed lines illustrate the spread of all models within 1σ of the best-fitting solution. SNL-1 is approximately isotropic in the central regions ($r < \theta_{\text{Ein}}$), while the outskirts are characterised by an intrinsically-oblate and anisotropic SVE.

ply in galaxy-scale lens systems, where internal structures such as bars could also play a role. Therefore, using the central velocity dispersion measurements as part of lens models would propagate this systematic bias and render the lensing sample non-representative. It is thus important to determine whether the selection function for lensing does indeed favour certain geometric configurations, and whether these configurations can be accurately reproduced in lens models.

It is to this end that dynamical models, such as those presented in this work, can provide insight. For example, the u parameter in this implementation of the Schwarzschild model describes the projection of a triaxial system. If strong lens galaxies have a tendency to be end-on triaxial systems, the distribution of u for a sample of lens galaxies will have a lower mean with respect to a mass-matched sample of non-lensed galaxies. Schwarzschild implementations which include treatment of figure rotation such as FORSTAND (Vasiliev et al. 2021) could simultaneously constrain the orientation of time-variable triaxial structures such as bars. However, as prefaced in Section 1, the sample of strong lens galaxies with spatially-resolved stellar kinematics of sufficient quality is currently too small for a statistical analysis. Exploiting the adaptive-optics capabilities of upcoming facilities such as MAVIS (McDermid et al. 2020) and HARMONI (Thatte et al. 2016) will bring more distant strong lens galaxies into the regime amenable to this analysis.

Although a direct statistical test is not yet available, the existing mass models used by lensing analyses appear to agree with independent techniques. For instance, results

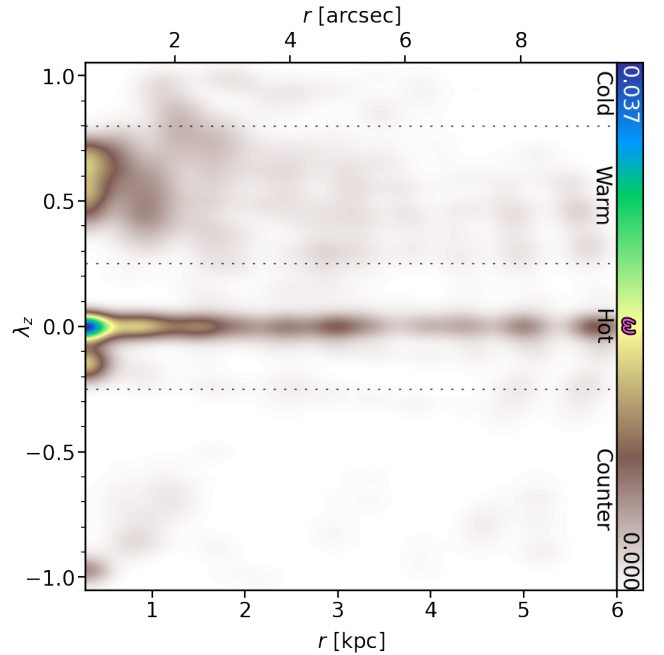


Figure 7. Circularity distribution of the best-fitting Schwarzschild model within the spectroscopic FOV. The colour shows the orbital weight as a function of circularity and radius. The black dashed lines show the separation into four broad dynamical components (see text). SNL-1 contains predominantly dynamically-hot orbits at all radii. The inner rotating ‘disk’ is visible for $r \lesssim 2\text{kpc}$ and $\lambda_z \sim 0.6$. There is also the suggestion of counter-rotating orbits, though these contribute little mass.

from lensing show that the total-mass distributions of the lensing population exhibit a surprisingly strong tendency towards isothermal radial profiles — having $\gamma \sim -2.1$ for $\rho_{\text{tot}}(r) \propto r^\gamma$ (e.g. Treu & Koopmans 2004; Koopmans et al. 2009; Auger et al. 2010; Barnabè et al. 2011; Bolton et al. 2012; Sonnenfeld et al. 2013; Shajib et al. 2021), with an intrinsic scatter of order 0.1–0.2 between them. This is in good agreement with direct modelling of the total mass distribution using Jeans models of the stellar kinematics (Tortora et al. 2014; Cappellari et al. 2015; Poci et al. 2017; Bellstedt et al. 2018; Li et al. 2019; Derkenne et al. 2021, despite different internal assumptions between them), cosmological simulations (Remus et al. 2013; Wang et al. 2019), and gas dynamical models (Serra et al. 2016), at least for $z \lesssim 0.5$ (Derkenne et al. 2021). Since these studies are on physically similar but non-lensed galaxies, this could imply at face value that there is no additional lensing selection bias beyond the velocity dispersion. However, by construction, assuming a single spherical power-law for the total mass of galaxies (or even an oblate total-mass distribution; Poci et al. 2017) can not account for triaxiality (or bars), and so this comparison can not exclude the existence of such a bias.

We can calculate the total-mass profile slope from the dynamical model in this work by simply combining the best-fitting stellar and DM contributions. This is given in Fig. 10, presented on the same scheme as Fig. 4. Given the flexibility of the models used in this work, there is no guarantee that the resulting total-mass density should be accurately described by a single power-law in radius. We therefore mea-

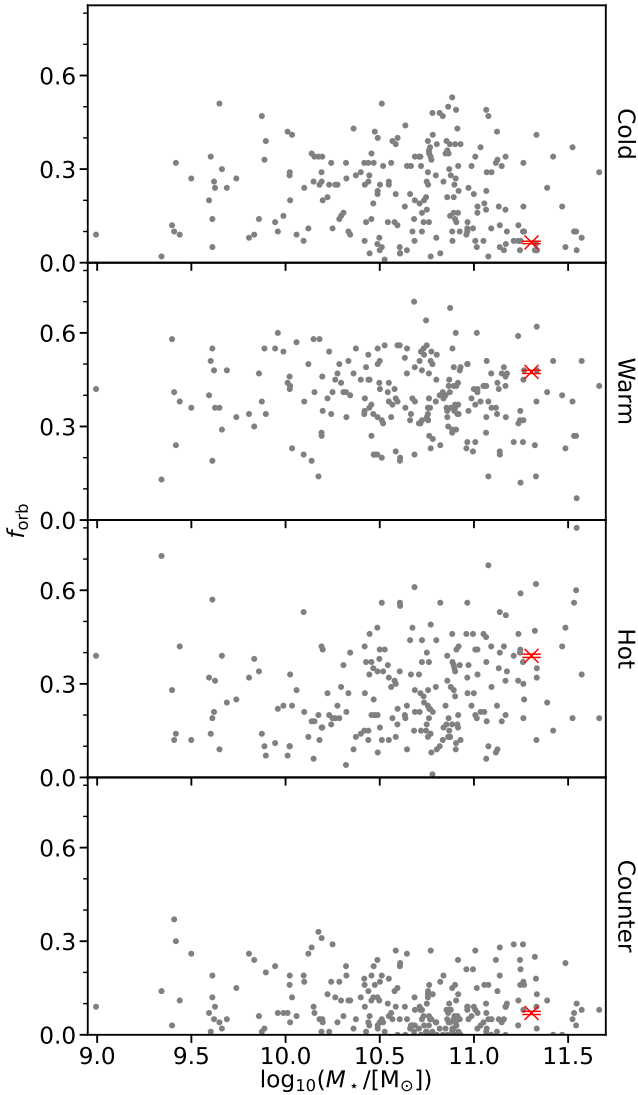


Figure 8. Orbit fractions as a function of stellar mass. The grey dots show the fractions of cold, warm, hot, and counter-rotating orbits (top to bottom) from [Zhu et al. \(2018b\)](#) for the CALIFA sample. The corresponding values from the dynamical model of SNL-1 are marked by the red crosses. The illustrated uncertainty is the spread of all models within 1σ of the best-fit.

sure the mean logarithmic density slope within R_e given as

$$\gamma' = \frac{\log_{10}[\rho_{\text{tot}}(R_e)/\rho_{\text{tot}}(R_{\text{in}})]}{\log_{10}(R_e/R_{\text{in}})} \quad (2)$$

where we set $R_{\text{in}} = 1''$, the FWHM of the kinematic data. We measure a mean logarithmic slope of the total-mass density profile to be $\gamma' = 2.262 \pm 0.006$ (1σ uncertainty), which is within the distributions found in the aforementioned works from lensing, stellar and gas kinematics, and cosmological simulations. While in this work we do not constrain the total-mass directly like previous studies, [Poci et al. \(2017\)](#) showed that modelling the total-mass directly or considering stellar+DM contributions produce consistent results, while [Barnabè et al. \(2011\)](#) showed that the slopes of the total-mass profiles between Jeans models and (two-integral) Schwarzschild models agree.

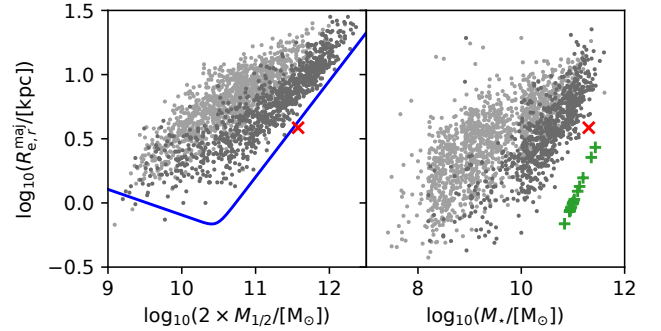


Figure 9. Mass-size plane projections for two different literature samples. *Left:* the dynamical mass and the effective radius along the major axis R_e^{maj} for the MaNGA sample ([Li et al. 2018](#)). $M_{1/2}$ is the dynamical mass enclosed within the 3D spherical half-light radius $R_{1/2}$. The blue line shows the “zone of exclusion” of [Cappellari et al. \(2013b\)](#). *Right:* the total stellar mass and the effective radius along the major axis R_e^{maj} for the GAMA subset (non-cluster galaxies) of the SAMI sample ([Croom et al. 2021](#)). The green plus symbols show the sample of ‘relic’ galaxies from the INSPIRE survey ([Spiniello et al. 2021](#)). In both panels, the samples are coloured by morphological type; late-type galaxies are light grey (‘S’ from MaNGA and `VisualMorphologyDR3.TYPE` ≥ 2.0 for SAMI), and earlier morphological types are dark grey. In both panels, the corresponding measurement from the dynamical model of SNL-1 is marked by the red cross. The sizes from both surveys are r -band measurements. We compute an r -band effective radius for SNL-1 from FORS2 photometry of $R_{e,r}^{\text{maj}} = 5.98''$ (3.83 kpc). In both panels, SNL-1 lies at the compact, high-mass edge of the general galaxy populations.

Finally more broadly, we have derived a measurement of M_{Ein} from the Schwarzschild model which is in excellent agreement with that from the independent lensing constraints. This result justifies being able to leverage lensing constraints directly within dynamical models. Doing so would be especially useful when constraints from the stellar kinematics alone are limited — for instance, at higher redshift. Requiring any model to respect both the enclosed lensing mass and the kinematic constraints simultaneously would also allow degeneracies to be mitigated concerning implied gradients in M/L , among others.

5.3 Exploring Different Orientations

The Schwarzschild model is fully defined in 3D space, and is projected through the LOS only to compare to observations. We are therefore able to ‘observe’ this model at arbitrary orientations. In this section we explore particular re-projections of the best-fit dynamical model, and their impact on the lensing properties. We show examples in [Fig. 11](#). These figures are constructed by taking the distribution of orbits and their relative weights from the original Schwarzschild model, then ‘observing’ the model from the specified viewing direction. New LOSVD are computed from this viewing direction. The surface brightness and kinematics are then measured by integrating, and fitting a Gauss-Hermite function to, these LOSVD, respectively. Since the models are spatially binned for the sole purpose of comparing to observations, we explore these re-projections on a non-binned pixel grid, but maintaining the MUSE pixel scale of 0.2 arcsec/pixel.

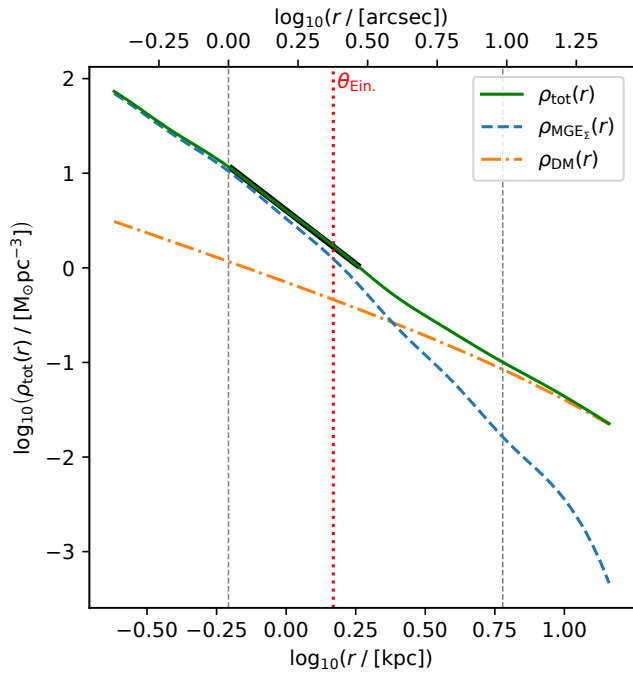


Figure 10. Density profiles for SNL-1 from the best-fit Schwarzschild model. The total enclosed mass is shown in green [given by $M_*(r) + M_{\text{DM}}(r)$], the stellar mass is dashed blue, and the DM is dot-dashed orange. Underplotted in the thick black line is the single power-law $\rho_{\text{tot}}(r) \propto r^{\gamma'}$ with the value of γ' measured from Eq. (2). SNL-1 does indeed have a mean logarithmic density slope which is close to isothermal over the fitted radial range. In addition, the black line illustrates that a power-law is a good representation of the total-mass density for SNL-1 over the region it is measured.

We explore two projections in addition to the observed direction in Fig. 11, defined by their viewing angles: from left to right, $(\theta, \phi, \psi) = (\theta', \phi', \psi')$; $(\theta, \phi, \psi) = (90^\circ, 0^\circ, \psi')$; $(\theta, \phi, \psi) = (0^\circ, 90^\circ, \psi')$. Primed angles refer to their observed values; that is, those derived from the best-fitting Schwarzschild model and given in Table 2. The additional projections correspond to what are expected to be the most and least dense along the LOS, and should therefore have the largest impact on the lensing cross-section. The kinematics exhibit changes which are expected for the different orientations; the edge-on projection shows the highest amplitude of rotation, which effectively vanishes in the face-on projection. The velocity dispersion also contains the signature of high rotation in the edge-on projection, with a depression along the mid-plane.

From the surface brightness of each projection, we compute the lensing cross-section by assuming a spatially-constant M_*/L , and neglecting the small DM contribution within θ_{Ein} . (discussed below). These are shown in Fig. 12. The face-on and edge-on/end-on projections exhibit a cross-section area which is $0.671\times$ and $1.165\times$ that of the observed projection. Conversely, we see only a $\sim 10\%$ change in θ_{Ein} between the extrema. The edge-on/end-on relative cross-section is perhaps unsurprising, since the best-fit dynamical model has a corresponding inclination of $\sim 88^\circ$. This implies that SNL-1 is already in a configuration which is close to its ‘maximum’ projection, and suggests that it was

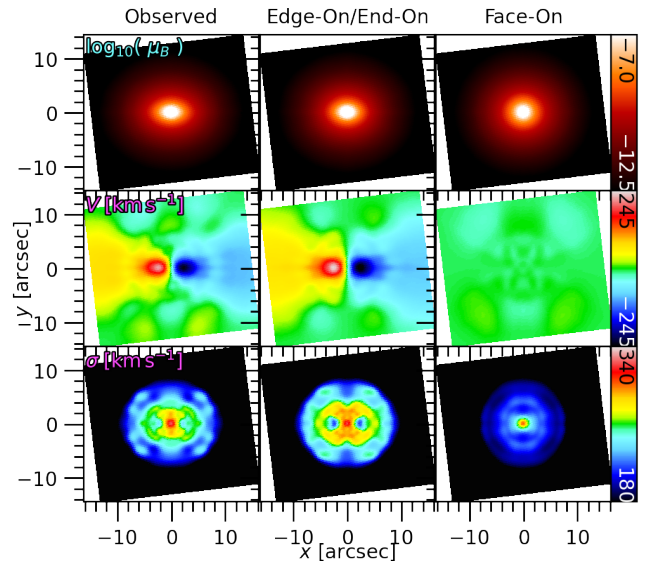


Figure 11. Re-projected Schwarzschild models of SNL-1. From top to bottom are the projected surface brightness, mean velocity, and velocity dispersion. From left to right, the viewing angles are: observed $(\theta, \phi, \psi) = (\theta', \phi', \psi')$; edge-on and end-on $(\theta, \phi, \psi) = (90^\circ, 0^\circ, \psi')$; face-on $(\theta, \phi, \psi) = (0^\circ, 90^\circ, \psi')$. The kinematics are shown simply for illustration, and align with the expectation for these viewing directions. The changes to the surface brightness (and correspondingly the mass density) allow us to probe the impact of particular viewing directions on the strength of the lensing signal.

detected as a lens in SNELLS at least partially due to its favourable orientation. Moreover, the substantial change in lensing cross-section and central velocity dispersion for the different projections, with little change to θ_{Ein} , might also produce different inferred mass profiles from lensing techniques which utilise the central kinematics (e.g. Treu et al. 2010).

Applying a spatially-constant M_*/L may impact the projected mass measurements for each orientation. We of course do not have access to the M_*/L integrated along lines-of-sight other than the observed orientation. However, the radial geometry of the observed M_*/L map (Fig. 2, inset) indicates that this geometry may hold for all projections. In that case, and since we are measuring the cross-sections relative to the observed orientation, applying the same $M_*/L(R)$ profile (such as the one measured in Fig. 2) to each projection will produce the same relative differences as a simple spatially-constant M_*/L . Similarly, given the spherical NFW employed in the dynamical model, the DM also does not have an impact on the relative measurements for the re-projections.

6 CONCLUSION

We have explored general orbit-based dynamical models of the relatively-nearby strong-lens system SNL-1. We have compared our results directly to the measurements from lensing models, and investigated a host intrinsic properties. Our findings are summarised here.

- The enclosed mass measurements between the dynamical

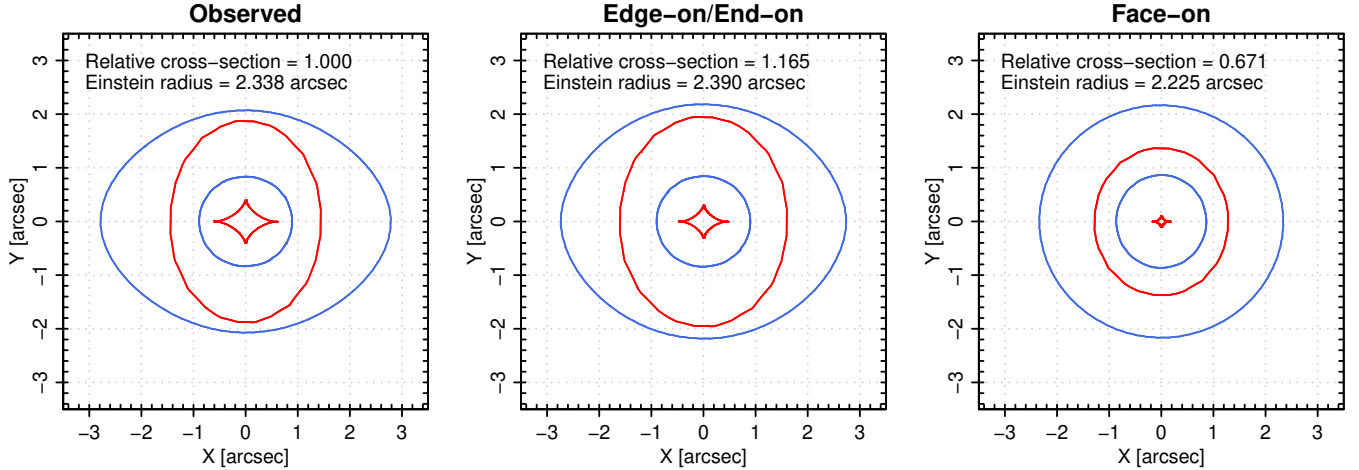


Figure 12. Lensing properties of SNL-1 for three different orientations, as computed from the re-projected dynamical models. From left to right is the observed, edge-on/end-on, and face-on projections. The surface densities have been rescaled to lensing convergence by a single constant factor which reproduces the observed Einstein radius in the observed orientation. The blue and red lines show the image-plane critical curves and source-plane caustics, respectively. The cross-section for lensing is given by the area inside the outer caustic: the cross section in the observed orientation is close to that of the “maximal-lensing” edge-on/end-on orientation, and substantially larger than the “minimal-lensing” face-on case.

and lensing models agree well within their respective uncertainties, with $M_{\text{Ein.}}^{\text{lens}}/M_{\text{Ein.}}^{\text{Schw.}} = 0.96$. This result supports the conclusion from the lensing model which favoured a relatively dwarf-poor IMF such as Kroupa (2001) for the centre of SNL-1 (Smith et al. 2015). We found that SNL-1 is baryon-dominated within the spectroscopic FOV, which encompasses both $\theta_{\text{Ein.}}$ and R_e (Fig. 4).

- SNL-1 appears to be oblate-triaxial and radially-anisotropic in its outer regions (Figures 5 and 6). In general, models (lensing or otherwise) which attempt to separate the baryonic and DM contributions to the total mass need to be able to account for these physical properties.
- Dynamically, SNL-1 is consistent with the broader galaxy population at fixed mass as traced by the CALIFA survey. Despite appearing to be a typical old, massive, red ETG, SNL-1 still exhibits relatively high rotation velocities in a central thick disk-like configuration. This is evidenced by the somewhat high proportion of kinematically-warm orbits within R_e (Fig. 8).
- In contrast, SNL-1 is markedly more compact at fixed mass compared to the MaNGA and (field) SAMI samples (Fig. 9). This compactness likely enhances the lensing signal compared to that of lower-density galaxies even at fixed mass. Nevertheless, the shape of the mass density profile of SNL-1 is in good agreement with a wide range of galaxy samples (Fig. 10).
- Finally, we explored the impact of changing the observed orientation of a galaxy which is already known to be a lens. We find a substantial impact on the lensing cross-section of a factor of ~ 2 between the projected extrema. We find only a minor difference between the observed and maximal orientations, implying that the selection of SNL-1 as a lens may have been impacted by its observed orientation (Fig. 12).

We conclude that combining lensing and sophisticated orbit-based dynamical models will provide access to the intrinsic physical properties of galaxies in a robust manner. In anticipation of the increase in the number of suitable galaxies

expected with upcoming facilities, we continue to investigate the ways in which lensing and dynamical analyses can complement one another.

ACKNOWLEDGEMENTS

Both authors are supported by the Science and Technology Facilities Council through the Durham Astronomy Consolidated Grant 2020–2023 (ST/T000244/1). This research is based on observations collected at the European Organisation for Astronomical Research in the Southern Hemisphere under ESO programme 0100.B-0769(A). This work used the DiRACDurham facility managed by the Institute for Computational Cosmology on behalf of the STFC DiRAC HPC Facility (www.dirac.ac.uk). The equipment was funded by BEIS capital funding via STFC capital grants ST/K00042X/1, ST/P002293/1, ST/R002371/1 and ST/S002502/1, Durham University and STFC operations grant ST/R000832/1. DiRAC is part of the National e-Infrastructure. This work also made use of the OzStar supercomputer at Swinburne University. This work utilised existing software packages for data analysis and presentation, including ASTROPY (Astropy Collaboration et al. 2013), CYTHON (Behnel et al. 2011), IPYTHON (Perez & Granger 2007), MATPLOTLIB (Hunter 2007), NUMPY (Harris et al. 2020), the SCIPY ecosystem (Virtanen et al. 2020), and STATSMODELS (Seabold & Perktold 2010). We finally thank the anonymous referee for comments which improved the clarity of this work.

DATA AVAILABILITY

The observational data used in this work are publicly available in the ESO archive (archive.eso.org). Other products can be provided upon reasonable request to the author.

REFERENCES

- Astropy Collaboration et al., 2013, *Astronomy and Astrophysics*, 558, A33
- Auger M. W., Treu T., Bolton A. S., Gavazzi R., Koopmans L. V. E., Marshall P. J., Moustakas L. A., Burles S., 2010, *The Astrophysical Journal*, Volume 724, Issue 1, pp. 511-525 (2010), 724, 511
- Barnabè M., Czoske O., Koopmans L. V. E., Treu T., Bolton A. S., Gavazzi R., 2009, *Monthly Notices of the Royal Astronomical Society*, 399, 21
- Barnabè M., Czoske O., Koopmans L. V. E., Treu T., Bolton A. S., 2011, *Monthly Notices of the Royal Astronomical Society*, 415, 2215
- Barone T. M., et al., 2021, arXiv:2107.01054 [astro-ph]
- Behnel S., Bradshaw R., Citro C., Dalcin L., Seljebotn D. S., Smith K., 2011, *Computing in Science Engineering*, 13, 31
- Bellstedt S., et al., 2018, *Monthly Notices of the Royal Astronomical Society*, 476, 4543
- Bender R., Burstein D., Faber S. M., 1992, *The Astrophysical Journal*, 399, 462
- Binney J., Tremaine S., 1987, *Galactic Dynamics*. Princeton University Press, Princeton, N.J
- Bohlin R. C., Gordon K. D., Tremblay P.-E., 2014, *Publications of the Astronomical Society of the Pacific*, 126, 711
- Bohlin R. C., Hubeny I., Rauch T., 2020, *The Astronomical Journal*, 160, 21
- Bolton A. S., Burles S., Koopmans L. V. E., Treu T., Moustakas L. A., 2006, *The Astrophysical Journal*, 638, 703
- Bolton A. S., et al., 2012, *The Astrophysical Journal*, 757, 82
- Bundy K., et al., 2015, *The Astrophysical Journal*, Volume 798, Issue 1, article id. 7, 24 pp. (2015), 798, 7
- Burstein D., Bender R., Faber S., Nolthenius R., 1997, *The Astronomical Journal*, 114, 1365
- Campbell L. A., et al., 2014, *Monthly Notices of the Royal Astronomical Society*, 443, 1231
- Campbell D. J. R., et al., 2017, *Monthly Notices of the Royal Astronomical Society*, 469, 2335
- Cappellari M., 2002, *Monthly Notices of the Royal Astronomical Society*, Volume 333, Issue 2, pp. 400-410., 333, 400
- Cappellari M., 2008, *Monthly Notices of the Royal Astronomical Society*, 390, 71
- Cappellari M., 2013, *The Astrophysical Journal*, 778, L2
- Cappellari M., 2017, *Monthly Notices of the Royal Astronomical Society*, Volume 466, Issue 1, p.798-811, 466, 798
- Cappellari M., Copin Y., 2003, *Monthly Notice of the Royal Astronomical Society*, Volume 342, Issue 2, pp. 345-354., 342, 345
- Cappellari M., et al., 2006, *Monthly Notices of the Royal Astronomical Society*, Volume 366, Issue 4, pp. 1126-1150., 366, 1126
- Cappellari M., et al., 2013a, *Monthly Notices of the Royal Astronomical Society*, Volume 432, Issue 3, p.1709-1741, 432, 1709
- Cappellari M., et al., 2013b, *Monthly Notices of the Royal Astronomical Society*, Volume 432, Issue 3, p.1862-1893, 432, 1862
- Cappellari M., et al., 2015, *The Astrophysical Journal Letters*, Volume 804, Issue 1, article id. L21, 7 pp. (2015), 804, L21
- Chae K.-H., 2003, *Monthly Notices of the Royal Astronomical Society*, 346, 746
- Colina L., Bohlin R. C., Castelli F., 1996, *The Astronomical Journal*, 112, 307
- Collier W. P., Smith R. J., Lucey J. R., 2018, *Monthly Notices of the Royal Astronomical Society*, 473, 1103
- Cortese L., et al., 2014, *The Astrophysical Journal*, 795, L37
- Croom S. M., et al., 2012, *Monthly Notices of the Royal Astronomical Society*, 421, 872
- Croom S. M., et al., 2021, *Monthly Notices of the Royal Astronomical Society*, p. stab229
- Czoske O., Barnabè M., Koopmans L. V. E., Treu T., Bolton A. S., 2008, *Monthly Notices of the Royal Astronomical Society*, 384, 987
- Dejonghe H., 1987, *Monthly Notices of the Royal Astronomical Society*, 224, 13
- Derkenne C., McDermid R. M., Poci A., Remus R.-S., Jørgensen I., Emsellem E., 2021, *Monthly Notices of the Royal Astronomical Society*, 506, 3691
- Emsellem E., Monnet G., Bacon R., Nieto J.-L., 1994, *Astronomy and Astrophysics*, 285, 739
- Falcón-Barroso J., Sánchez-Blázquez P., Vazdekis A., Ricciardelli E., Cardiel N., Cenarro A. J., Gorgas J., Peletier R. F., 2011, *Astronomy & Astrophysics*, 532, A95
- Franx M., Illingworth G., de Zeeuw T., 1991, *The Astrophysical Journal*, 383, 112
- Gallazzi A., Charlot S., Brinchmann J., White S. D. M., Tremonti C. A., 2005, *Monthly Notices of the Royal Astronomical Society*, 362, 41
- Harris C. R., et al., 2020, *Nature*, 585, 357
- Helmi A., Babusiaux C., Koppelman H. H., Massari D., Veljanoski J., Brown A. G. A., 2018, *Nature*, 563, 85
- Hunter J. D., 2007, *Computing in Science and Engineering*, vol. 9, no. 3, pp. 90-95, 9, 90
- Jin Y., Zhu L., Long R. J., Mao S., Xu D., Li H., van de Ven G., 2019, *Monthly Notices of the Royal Astronomical Society*, 486, 4753
- Jin Y., Zhu L., Long R. J., Mao S., Wang L., van de Ven G., 2020, *Monthly Notices of the Royal Astronomical Society*, 491, 1690
- Karademir G. S., Remus R.-S., Burkert A., Dolag K., Hoffmann T. L., Moster B. P., Steinwandel U. P., Zhang J., 2019, *Monthly Notices of the Royal Astronomical Society*, 487, 318
- Khochfar S., et al., 2011, *Monthly Notices of the Royal Astronomical Society*, 417, 845
- Komatsu E., et al., 2011, *The Astrophysical Journal Supplement Series*, 192, 18
- Koopmans L. V. E., et al., 2009, *The Astrophysical Journal*, 703, L51
- Kormendy J., Ho L. C., 2013, *Annual Review of Astronomy and Astrophysics*, 51, 511
- Krajnović D., Emsellem E., den Brok M., Marino R. A., Schmidt K. B., Steinmetz M., Weilbacher P. M., 2018, *Monthly Notices of the Royal Astronomical Society*, 477, 5327
- Kroupa P., 2001, *Monthly Notices of the Royal Astronomical Society*, 322, 231
- La Barbera F., et al., 2019, *Monthly Notices of the Royal Astronomical Society*, 489, 4090
- Lackner C. N., Cen R., Ostriker J. P., Joung M. R., 2012, *Monthly Notices of the Royal Astronomical Society*, 425, 641
- Lawson C. L., Hanson R. J., 1995, *Solving Least Squares Problems*. Classics in Applied Mathematics, Society for Industrial and Applied Mathematics, doi:10.1137/1.9781611971217
- Li H., et al., 2017, *The Astrophysical Journal*, 838, 77
- Li H., et al., 2018, *Monthly Notices of the Royal Astronomical Society*, 476, 1765
- Li R., et al., 2019, *Monthly Notices of the Royal Astronomical Society*, 490, 2124
- McDermid R. M., et al., 2020, arXiv e-prints, 2009, arXiv:2009.09242
- Mitzkus M., Cappellari M., Walcher C. J., 2017, *Monthly Notices of the Royal Astronomical Society*, 464, 4789
- Monnet G., Bacon R., Emsellem E., 1992, *Astronomy and Astrophysics*, 253, 366
- Naab T., Khochfar S., Burkert A., 2006, *The Astrophysical Journal*, 636, L81
- Navarro J. F., Frenk C. S., White S. D. M., 1996, *The Astrophysical Journal*, 462, 563
- Newman A. B., Smith R. J., Conroy C., Villaume A., van Dokkum P., 2017, *The Astrophysical Journal*, 845, 157

Newton E. R., Marshall P. J., Treu T., Auger M. W., Gavazzi R., Bolton A. S., Koopmans L. V. E., Moustakas L. A., 2011, *The Astrophysical Journal*, 734, 104

Oser L., Ostriker J. P., Naab T., Johansson P. H., Burkert A., 2010, *The Astrophysical Journal*, 725, 2312

Perez F., Granger B. E., 2007, *Computing in Science Engineering*, 9, 21

Pietrinferni A., Cassisi S., Salaris M., Castelli F., 2004, *The Astrophysical Journal*, 612, 168

Poci A., Cappellari M., McDermaid R. M., 2017, *Monthly Notices of the Royal Astronomical Society*, 467, 1397

Remus R.-S., Burkert A., Dolag K., Johansson P. H., Naab T., Oser L., Thomas J., 2013, *The Astrophysical Journal*, 766, 71

Rodriguez-Gomez V., et al., 2016, *Monthly Notices of the Royal Astronomical Society*, 458, 2371

Sánchez-Blázquez P., et al., 2006, *Monthly Notices of the Royal Astronomical Society*, 371, 703

Sánchez S. F., et al., 2012, *Astronomy & Astrophysics*, 538, A8

Schaller M., et al., 2015, *Monthly Notices of the Royal Astronomical Society*, 452, 343

Schlafly E. F., Finkbeiner D. P., 2011, *The Astrophysical Journal*, 737, 103

Schwarzschild M., 1979, *Astrophysical Journal, Part 1, vol. 232, Aug. 15, 1979, p. 236-247.*, 232, 236

Scott N., et al., 2017, *Monthly Notices of the Royal Astronomical Society*, 472, 2833

Seabold S., Perktold J., 2010, in Python in Science Conference. Austin, Texas, pp 92–96, doi:10.25080/Majora-92bf1922-011

Serra P., Oosterloo T., Cappellari M., den Heijer M., Józsa G. I. G., 2016, *Monthly Notices of the Royal Astronomical Society*, 460, 1382

Shajib A. J., Treu T., Birrer S., Sonnenfeld A., 2021, *Monthly Notices of the Royal Astronomical Society*, 503, 2380

Shu Y., et al., 2015, *The Astrophysical Journal*, 803, 71

Smith R. J., Lucey J. R., Conroy C., 2015, *Monthly Notices of the Royal Astronomical Society*, 449, 3441

Smith R. J., Lucey J. R., Collier W. P., 2018, *Monthly Notices of the Royal Astronomical Society*, 481, 2115

Sonnenfeld A., Treu T., Gavazzi R., Suyu S. H., Marshall P. J., Auger M. W., Nipoti C., 2013, *The Astrophysical Journal, Volume 777, Issue 2, article id. 98, 15 pp. (2013).*, 777, 98

Spiniello C., Barnabè M., Koopmans L. V. E., Trager S. C., 2015, *Monthly Notices of the Royal Astronomical Society: Letters*, 452, L21

Spiniello C., et al., 2021, arXiv:2103.12086 [astro-ph]

Thatte N. A., et al., 2016, in Ground-Based and Airborne Instrumentation for Astronomy VI. International Society for Optics and Photonics, p. 99081X, doi:10.1117/12.2230629

Thomas J., et al., 2011, *Monthly Notices of the Royal Astronomical Society, Volume 415, Issue 1, pp. 545-562.*, 415, 545

Tian Y., Cheng H., McGaugh S. S., Ko C.-M., Hsu Y.-H., 2021, *The Astrophysical Journal Letters*, 917, L24

Tortora C., La Barbera F., Napolitano N. R., Romanowsky A. J., Ferreras I., de Carvalho R. R., 2014, *Monthly Notices of the Royal Astronomical Society, Volume 445, Issue 1, p.115-127,* 445, 115

Treu T., 2010, *Annual Review of Astronomy and Astrophysics*, 48, 87

Treu T., Koopmans L. V. E., 2004, *The Astrophysical Journal*, 611, 739

Treu T., Auger M. W., Koopmans L. V. E., Gavazzi R., Marshall P. J., Bolton A. S., 2010, *The Astrophysical Journal, Volume 709, Issue 2, pp. 1195-1202 (2010).*, 709, 1195

Vasiliev E., Belokurov V., Erkal D., 2021, *Monthly Notices of the Royal Astronomical Society*, 501, 2279

Vaughan S. P., Davies R. L., Zieleniewski S., Houghton R. C. W., 2018, *Monthly Notices of the Royal Astronomical Society*, 475, 1073

Σ_* [M_\odot/pc^2]	μ_B [L_\odot/pc^2]	σ [arcsec]	q
665,322.22	111,570.70	0.022	0.700
241,694.28	40,530.74	0.075	0.500
66,986.41	11,235.65	0.093	0.900
109,985.28	18,455.82	0.212	0.900
21,783.49	3,657.34	0.491	0.900
43,580.97	7,328.28	0.612	0.503
21,490.22	3,619.68	1.279	0.500
6,248.14	1,053.47	1.396	0.812
3,028.55	520.74	2.268	0.517
3,128.43	551.26	3.426	0.740
712.15	135.44	8.168	0.846

Table A1. MGE $_\Sigma$ and MGE $_\mu$ for SNL-1. The columns represent, from left to right, the projected surface mass density, projected surface brightness, width (peak location), and axis ratio, respectively. By construction (Section 3.1), the Gaussians for both MGE models have the same widths and axis ratios. Moreover, all Gaussian components have the same fixed PA.

Vazdekis A., Koleva M., Ricciardelli E., Röck B., Falcón-Barroso J., 2016, *Monthly Notices of the Royal Astronomical Society*, 463, 3409

Virtanen P., et al., 2020, *Nature Methods*, 17, 261

Wang Y., et al., 2019, *Monthly Notices of the Royal Astronomical Society*, 490, 5722

Weijmans A.-M., et al., 2014, *Monthly Notices of the Royal Astronomical Society*, 444, 3340

Wolf J., Martinez G. D., Bullock J. S., Kaplinghat M., Geha M., Muñoz R. R., Simon J. D., Avedo F. F., 2010, *Monthly Notices of the Royal Astronomical Society*, 406, 1220

Yang M., Zhu L., Weijmans A.-M., van de Ven G., Boardman N., Morganti R., Oosterloo T., 2020, *Monthly Notices of the Royal Astronomical Society*, 491, 4221

Zhu L., et al., 2018a, *Monthly Notices of the Royal Astronomical Society*, 473, 3000

Zhu L., van de Ven G., Méndez-Abreu J., Obreja A., 2018b, *Monthly Notices of the Royal Astronomical Society*, 479, 945

de Zeeuw T., Schwarzschild M., 1989, *The Astrophysical Journal*, 345, 84

van Dokkum P., Conroy C., Villaume A., Brodie J., Romanowsky A. J., 2017, *The Astrophysical Journal*, 841, 68

van de Ven G., De Zeeuw P. T., Van Den Bosch R. C. E., 2008, *Monthly Notices of the Royal Astronomical Society*, 385, 614

van den Bosch R. C. E., van de Ven G., Verolme E. K., Cappellari M., De Zeeuw P. T., 2008, *Monthly Notices of the Royal Astronomical Society*, 385, 647

APPENDIX A: PROJECTED DENSITY MODELS

Table A1 presents both the stellar mass density and luminosity density MGE models for SNL-1. For the models in this work, the MGEs are assumed to be axisymmetric in projection, and so all components have the same position angle.

APPENDIX B: SCHWARZSCHILD MODEL PARAMETER-SPACE EXPLORATION

Owing to the computationally-expensive implementations of the Schwarzschild technique, sampling methods such as Marko Chain Monte Carlo are currently impractical for

model selection. The exploration of the parameter-space is instead achieved with a grid search over reasonable parameter ranges. In the case of the q shape parameter, its maximum value is constrained by the flattening of the MGE model (van den Bosch et al. 2008). The search is initialised over a wide range in each parameter to avoid local minima, then follows the minimum χ^2 while iteratively decreasing the step size. The search terminates once all surrounding models produce worse fits to the data. The search over the parameter-space is shown in Fig. B1. This flexible grid approach still allows for the characterisation of the parameter-space, in particular any degeneracies between parameters, despite its relative simplicity.

The goodness-of-fit metric used here is a re-normalised version of the χ^2 . The normalisation is a factor of $\sqrt{2 \times N_{\text{obs}} \times N_{\text{GH}}}$, where N_{obs} is the number of spatial bins, and N_{GH} is the number of kinematic moments fit by the model (four in this work; Section 2.2) — see Zhu et al. (2018a) for further discussion on the goodness-of-fit. In order to estimate the uncertainties of the model parameters (Table 2), we take all models within 1σ given by this normalised metric, and for each parameter compute the standard deviation marginalised over all other parameters.

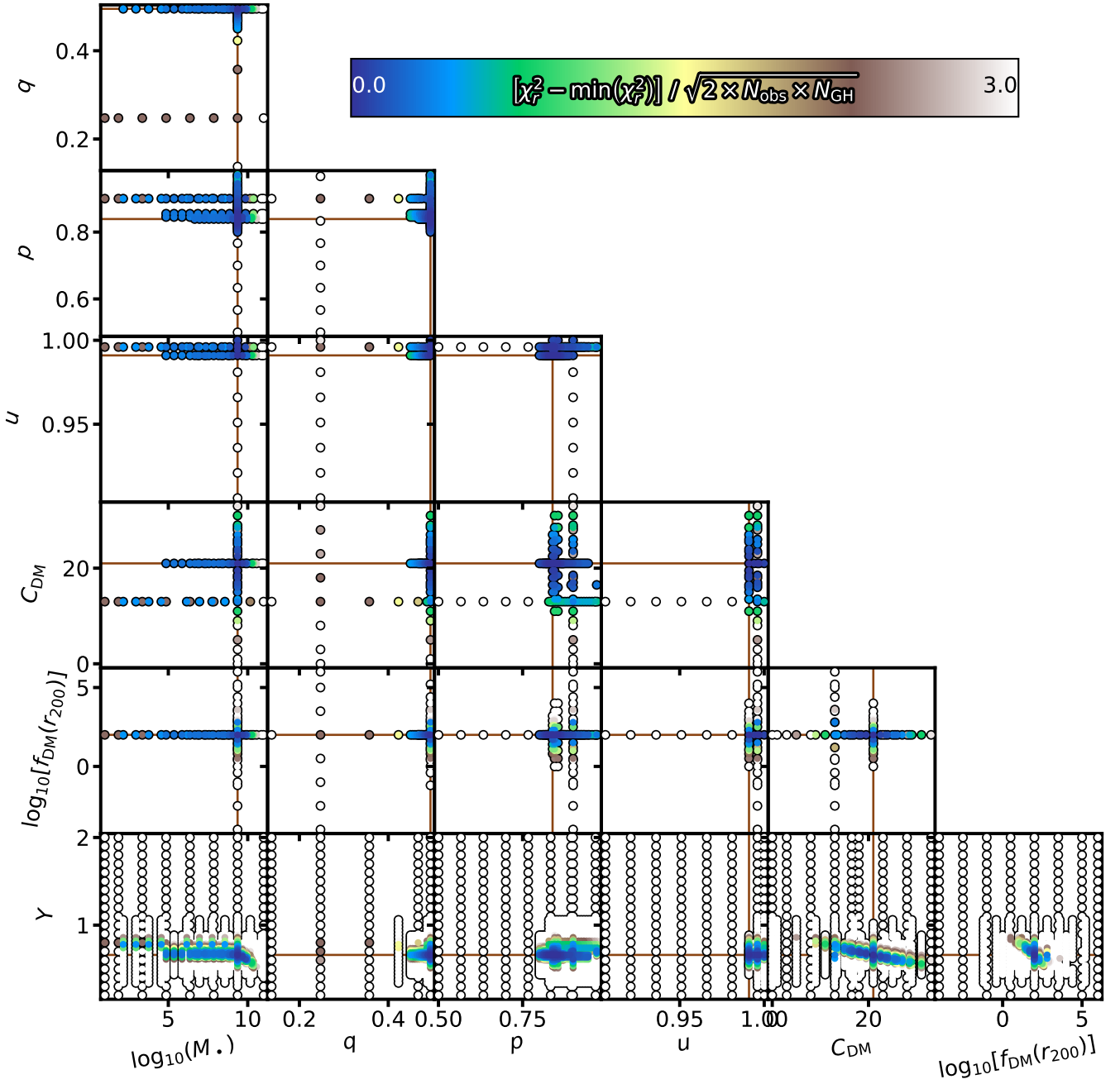


Figure B1. Schwarzschild model parameter-space, showing the exploration of all free parameters. Each model is shown as a point, coloured by its reduced χ^2 . The best-fit values are denote by the brown lines.